A polarimetric target detector using the Huynen fork

A Polarimetric Target Detector Using the Huynen Fork

A. Marino, S. R. Cloude, I. H. Woodhouse.

***Abstract*—The contribution of SAR polarimetry in target detection is described and found to add valuable information. A new target detection methodology is described that makes novel use of the polarization fork of the target. The detector is based on a correlation procedure in the target space, and other target representations (e.g. Huynen parameters or α angle) can be employed. The mathematical formulation is general and can be applied to any kind of single target, however in this paper the detection is optimized for the odd and even-bounces (first two elements of the Pauli scattering vector) and oriented dipoles. Validation against real data shows significant agreement with the expected results based on the theoretical description.**

***Index Terms*—Synthetic Aperture Radar (SAR), Polarimetry, Target Detection, Polarization Fork, Target Recognition.**

I. INTRODUCTION

THE ability of Synthetic Aperture Radar (SAR) to image through cloud cover and without solar illumination, in addition to its ability to partially penetrate foliage cover (dependent upon the wavelength), has established it as a powerful technique for target detection [1, 2]. In the last decade, attention has also been given to the examination of how the polarization of the signal may further develop this performance [3-7]. The aim of this study is target detection exploiting a particular aspect of the polarimetric target response, namely the polarization fork, of the targets. The detector is not based on a statistical technique, but rather a physical approach based on sensitivity of the polarimetric complex coherence to changes in polarization.

The approach is based on the potential to extract the target of interest in the target complex space. For this reason, full polarimetric data are required, because they represent a basis for the target space [8, 9]. In some way, it acts not dissimilarly to a decomposition theorem [10], however it is aimed more towards the detection of a chosen single target type rather than the breakdown of the partial target in predefined components.

The algorithm proposed is mainly focused on the detection of single (or simple) targets that can be completely characterized by one Sinclair (scattering) matrix [11-13]. In the case of a monostatic sensor and reciprocity of the medium the Sinclair matrix is symmetric and can be characterized by 6 parameters [13-15]:

$$[S]=[R(\phi_m)][T(\tau_m)][S_d][T(\tau_m)][R(-\phi_m)]$$

$$[S_d]=\begin{pmatrix} me^{i(\upsilon+\zeta)} & 0 \\ 0 & m\tan(\gamma)e^{-i(\upsilon-\zeta)} \end{pmatrix}$$

$$[T(\tau_m)]=\begin{pmatrix} \cos\tau_m & -i\sin\tau_m \\ -i\sin\tau_m & \cos\tau_m \end{pmatrix} \quad (1)$$

$$[R(\phi_m)]=\begin{pmatrix} \cos\phi_m & -\sin\phi_m \\ \sin\phi_m & \cos\phi_m \end{pmatrix}$$

In the work of Huynen [13] these parameters are linked to phenomenological aspects of the target. ϕ_m and τ_m are orientation angle and ellipticity angle of the target, and m, υ, γ and ζ are respectively, target magnitude, target skip angle, characteristic angle and absolute phase. Only 5 of them are sufficient to characterize a target, since the target absolute phase ζ can be neglected in single pass polarimetry (note that ζ is not negligible in polarimetric interferometry).

These parameters are related with the characteristic polarizations in the projective space of the Poincaré sphere and can be represented by the Polarization Fork (PF) [11, 16, 17]. The PF is mainly composed of X-pol Nulls, Co-pol Nulls and X-pol Max. The X-pol Nulls are polarizations that when transmitted do not have any return in the cross polarization (optimum polarizations). On the other hand, the Co-pol Nulls when transmitted do not have any return in the co-polarization. Finally, the X-pol Max when transmitted have maximum cross-polarization return. The X-pol Nulls, Co-pol Nulls and X-pol Max can always be visualized on the Poincaré sphere on the same plane (they form a fork shape). The reason why the PF is utilized is because it can represent physical target characteristics based on the location of the nulls. Figure 1 represents the PF illustrating the link with 4 Huynen parameters (absolute magnitude and phase are not represented on the Poincaré sphere). Where X_1, X_2 are X-pol Nulls, C_1, C_2 are Co-pol Nulls and S_1, S_2 are X-pol Max.

The matrix representation (Sinclair matrix) can be modified as a vectorial one [18, 19]:

$$\underline{k}=\frac{1}{2}Trace([S]\Psi)=[k_1,k_2,k_3,k_4]^T, \quad (2)$$

where *Trace*(.) is the sum of the diagonal elements of the matrix inside and Ψ is a complete set of 2x2 basis matrices under a Hermitian inner product. In the case of reciprocal

Manuscript received XXX, 2009. The work reported in this paper was conducted as a part of the SARTOM project led by eOsphere Limited and funded by the Electro-Magnetic Remote Sensing – Defence Technology Centre (EMRS-DTC), contract number EMRS/DTC/4/90.

A. Marino is with The University of Edinburgh (Tel. +44-131 650 2532; e-mail: a.marino@ ed.ac.uk).

S. R. Cloude is with AEL Consultants, Edinburgh, UK (Tel. +44-131 2483777; e-mail: aelc@mac.com)

I. H. Woodhouse is with The University of Edinburgh (Tel. +44-131 650 2527; Fax: +44-131 650 2524; e-mail: i.h.woodhouse@ ed.ac.uk).

medium and monostatic sensor, $\underline{k}$ is three dimensional complex (*SU*(3)) [20]. Finally, it is possible to define the scattering mechanism (weight vector) as a normalized vector $\underline{\omega} = \underline{k}/|\underline{k}|$. It is always possible to construct $\underline{\omega}$ starting from its PF.

Beside the PF and Huynen parameters, other kinds of parameterizations are possible, as long as the scattering mechanism can be reconstructed. In this context, a largely used procedure employs the α angle [21]:

$$\underline{\omega} = \left[\cos\alpha, \sin\alpha\cos\beta e^{i\varepsilon}, \sin\alpha\sin\beta e^{i\mu}\right]^T, \quad (3)$$

where α is a characteristic angle (different from γ) and β is dependent on the orientation of the target about the radar line of sight [21].

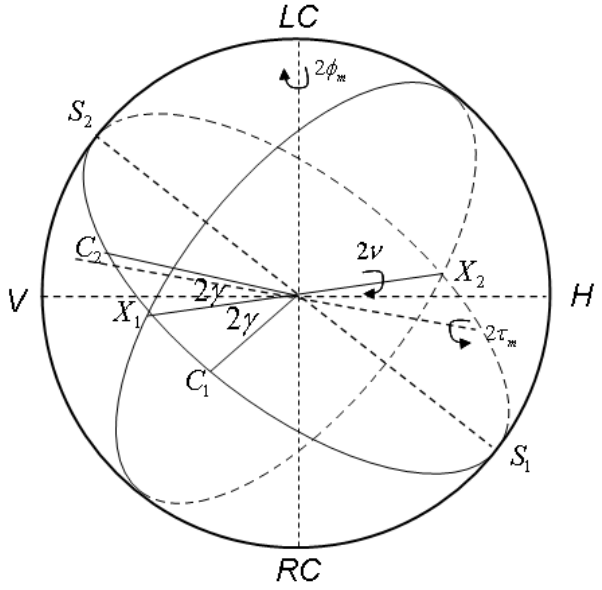

Figure 1. PF and relationship with Huynen parameters.

The target observed by a SAR system is not an idealized scattering target, but a combination of different targets which we refer to as a partial target [22-24]. Decomposition theorems are able to represent the partial target as a combination of idealized single target components [10]. In order to characterize a partial target the single scattering matrix is not sufficient since the partial target is a stochastic process and the second order statistics are required. In this context the target coherency matrix can be estimated:

$$[C] = \left\langle \underline{k} \cdot \underline{k}^{*T} \right\rangle, \quad (4)$$

where $\langle . \rangle$ is the finite averaging operator. (Note, we are not employing interferometry, but rather a single flight pass). A classical formulation is when $\underline{k}$ is expressed in Pauli basis (i.e. $\underline{k}_P = 1/\sqrt{2}\left[S_{HH} + S_{VV}, S_{HH} - S_{VV}, 2S_{HV}\right]^T$ where *H* is for horizontal and *V* vertical), or in Lexicographic basis (i.e. $\underline{k}_L = \left[S_{HH}, \sqrt{2}S_{HV}, S_{VV}\right]^T$). In general, if the scattering vector in a generic basis is $\underline{k} = \left[k_1, k_2, k_3\right]^T$, where k_1, k_2 and k_3 are complex numbers, the coherency matrix is:

$$[C] = \begin{bmatrix} \langle |k_1|^2 \rangle & \langle k_1 k_2^* \rangle & \langle k_1 k_3^* \rangle \\ \langle k_2 k_1^* \rangle & \langle |k_2|^2 \rangle & \langle k_2 k_3^* \rangle \\ \langle k_3 k_1^* \rangle & \langle k_3 k_2^* \rangle & \langle |k_3|^2 \rangle \end{bmatrix} \quad (5)$$

The methodology of this paper takes advantage of the polarimetric coherence [25]. If two different scattering mechanisms $\underline{\omega}_1$ and $\underline{\omega}_2$ are considered, the polarimetric coherence is:

$$\gamma = \frac{\langle i(\underline{\omega}_1) \cdot i^*(\underline{\omega}_2) \rangle}{\sqrt{\langle i(\underline{\omega}_1) \cdot i^*(\underline{\omega}_1) \rangle \langle i(\underline{\omega}_2) \cdot i^*(\underline{\omega}_2) \rangle}}, \quad (6)$$

where *i* is the image evaluated as

$$i(\underline{\omega}_j) = \underline{\omega}_j^{*T} \cdot \underline{k} \quad \text{with} \quad j = 1,2 \,. \quad (7)$$

In terms of the target coherency matrix, the polarimetric coherence is:

$$\gamma = \frac{\underline{\omega}_1^{*T} \langle [C] \rangle \underline{\omega}_2}{\sqrt{\underline{\omega}_1^{*T} \langle [C] \rangle \underline{\omega}_1 \cdot \underline{\omega}_2^{*T} \langle [C] \rangle \underline{\omega}_2}} \quad (8)$$

Please note this coherence is only polarimetric and not interferometric.

II. METHODOLOGY

Any (normalized) single target can be represented uniquely in the target space by a scattering mechanism $\underline{\omega}$. The image obtained with eq.7 evaluates the scalar projection of the observed target $\underline{k}$ on the scattering mechanism to be detected $\underline{\omega}_j$ (e.g. sphere, dipole, etc.). When the two images $i(\underline{\omega}_1)$ and $i(\underline{\omega}_2)$ are similar, the amplitude of the polarimetric coherence γ (eq.6) is high (by definition).

We want to demonstrate: *Given a scattering mechanism* $\underline{\omega}_1$ *proportional to the target to be detected, and given a second scattering mechanism* $\underline{\omega}_2$ *close to* $\underline{\omega}_1$ *within the target space, the polarimetric coherence is high if in the averaging cell the component of interest (proportional to* $\underline{\omega}_1$*) is stronger than the other two orthogonal components.*

1) In order to demonstrate the hypothesis, the first step is to define a basis for the target space where the target of interest is limited to just one component of the 3 dimensional complex vector $\underline{k}$. Geometrically, this operation can be accomplished with a change of basis using a unitary matrix, which set one axis exactly over the target of interest. In the following, the scattering mechanism after the change of basis is referred to as $\underline{\omega}_T = [1,0,0]^T$. $\underline{\omega}_T$ is the single target we want to detect (following the initial thesis $\underline{\omega}_1 = \underline{\omega}_T$). The coherence matrix [*C*] will be calculated starting from this new basis. The resulting image when the target $\underline{\omega}_T$ is selected is

$$i(\underline{\omega}_T) = k_1 \,. \quad (9)$$

In eq.9, the other two components of the scattering vector (i.e.

k_2 and k_3) are deleted completely. The projection of $\underline{k}$ over $\underline{\omega}_T$ selects the component of interest in the partial target, hence the target to detect is just in the k_1 component. For this reason, (in the new basis that sets $\underline{\omega}_T = [1,0,0]^T$) k_2 and k_3 are considered as *clutter*.

2) Secondly, the scattering mechanism $\underline{\omega}_2$ must be constructed close to $\underline{\omega}_T$. The latter is named the "pseudo-target", $\underline{\omega}_P$ (i.e. $\underline{\omega}_2 = \underline{\omega}_P$). $\underline{\omega}_P$ is obtained by moving slightly the entire polarization fork, since a slightly different polarization fork characterizes a slightly different target. In a first attempt, the small rotation of the characteristic polarizations on the Poincaré sphere can be accomplished using the Huynen parameters. In other words, in eq.1, ϕ_m, τ_m, υ and γ are substituted with $\phi_m \pm \Delta\phi_m$, $\tau_m \pm \Delta\tau_m$, $\upsilon \pm \Delta\upsilon$ and $\gamma \pm \Delta\gamma$, where $\Delta\phi_m$, $\Delta\tau_m$, $\Delta\upsilon$ and $\Delta\gamma$ are positive real numbers corresponding to a fraction (e.g. a twelfth or a tenth) of the maximum value of the co respective variable. The variation can be positive or negative in order to keep the final variable within the allowed range of values. For the pseudo-target, Eq.1 becomes:

$$[S_P] = [R(\phi_m + \Delta\phi_m)][T(\tau_m + \Delta\tau_m)][S_d][T(\tau_m + \Delta\tau_m)][R(-(\phi_m + \Delta\phi_m)]$$
$$[S_d] = \begin{pmatrix} e^{i(\upsilon+\Delta\upsilon)} & 0 \\ 0 & \tan(\gamma+\Delta\gamma)e^{-i(\upsilon+\Delta\upsilon)} \end{pmatrix} \quad (10)$$

Consequently, $[S_T] \approx [S_P]$, where $[S_T]$ is the scattering matrix of the target to detect (i.e. eq.1 with $m=1$ and $\varsigma = 0$). Similarly, $\underline{\omega}_P$ can be obtained starting from the α angle parameterization as:

$$\underline{\omega}_T = \left[\cos\alpha, \sin\alpha\cos\beta e^{i\varepsilon}, \sin\alpha\sin\beta e^{i\mu}\right]^T$$
$$\underline{\omega}_P = \begin{bmatrix} \cos(\alpha+\Delta\alpha) \\ \sin(\alpha+\Delta\alpha)\cos(\beta+\Delta\beta)e^{i(\varepsilon+\Delta\varepsilon)} \\ \sin(\alpha+\Delta\alpha)\sin(\beta+\Delta\beta)e^{i(\mu+\Delta\mu)} \end{bmatrix} \quad (11)$$

where again $\Delta\alpha$, $\Delta\beta$, $\Delta\varepsilon$ and $\Delta\mu$ are a fraction of the maximum value of co respective variables (in case of ε and μ the maximum value is fixed to 2π). Again, $\underline{\omega}_T \approx \underline{\omega}_P$.

In both the parameterisations, the components of the scattering mechanism are not linearly linked with the parameters. However fortunately they are continuous functions; when the parameters are selected in the allowed range of values (i.e. products of continuous functions). This guarantees that if the parameter variation is small enough, the change in the pseudo-target will be small as well. The optimization of the variations in order to have valuable pseudo target components is studied in the following sections. Once obtained the expression of $\underline{\omega}_P$ in the basis used by the parameterization (e.g. Pauli for α), the same change of basis that makes $\underline{\omega}_T = [1,0,0]^T$ is performed over $\underline{\omega}_P$. Consequently, $\underline{\omega}_P = [a,b,c]^T$, with a, b and c complex numbers. Considering $\underline{\omega}_T \approx \underline{\omega}_P$, we have $|a| \approx 1$, $|b| \approx 0$ and $|c| \approx 0$.

In order to show the relationship with the Huynen parameters, the scattering mechanism for the target of interest can be calculated as:

$$\underline{\omega}_T = \frac{1}{2}[U(\varphi,\vartheta,\delta)]Trace([S(\phi_m,\tau_m,\gamma,\upsilon)]\Psi) = [1,0,0]^T \quad (12)$$

where [*S*] is calculated from eq.1 (the brackets show the dependence to the Huynen parameters). The [*U*] matrix performs the change of basis that makes $\underline{\omega}_T = [1,0,0]^T$. [*U*] depends on two rotation angles and a change of phase (i.e. $\varphi, \vartheta, \delta$). The pseudo target can be calculated with a slightly change of the Huynen parameters:

$$\underline{\omega}_P = \frac{1}{2}[U(\varphi,\vartheta,\delta)]\cdot$$
$$\cdot Trace([S(\phi_m+\Delta\phi_m,\tau_m+\Delta\tau_m,\gamma+\Delta\gamma,\upsilon+\Delta\upsilon)]\Psi) = \quad (13)$$
$$= [a,b,c]^T$$

Hence, if $\Delta\phi_m = \Delta\tau_m = \Delta\upsilon = \Delta\gamma = 0$, than $\underline{\omega}_T = \underline{\omega}_P$, on the other hand if the variations are small the two scattering mechanisms start to be different, introducing the required distance.

3) Once the two scattering mechanisms are defined the polarimetric coherence (in the new basis) can be estimated from:

$$\gamma(\underline{\omega}_T, \underline{\omega}_P) = \frac{\langle i(\underline{\omega}_T)\cdot i^*(\underline{\omega}_P)\rangle}{\sqrt{\langle i(\underline{\omega}_T)\cdot i^*(\underline{\omega}_T)\rangle\langle i(\underline{\omega}_P)\cdot i^*(\underline{\omega}_P)\rangle}} \quad (14)$$

where:

$$\langle i(\underline{\omega}_T)\cdot i^*(\underline{\omega}_P)\rangle = a\langle|k_1|^2\rangle + b\langle k_1\cdot k_2^*\rangle + c\langle k_1\cdot k_3^*\rangle$$
$$\langle i(\underline{\omega}_T)\cdot i^*(\underline{\omega}_T)\rangle = \langle|k_1|^2\rangle \quad (15)$$
$$\langle i(\underline{\omega}_P)\cdot i^*(\underline{\omega}_P)\rangle = |a|^2\langle|k_1|^2\rangle + |b|^2\langle|k_2|^2\rangle + |c|^2\langle|k_3|^2\rangle +$$
$$+ 2\,\mathrm{Re}(ab^*\langle k_1\cdot k_2^*\rangle) + 2\,\mathrm{Re}(ac^*\langle k_1\cdot k_3^*\rangle) + 2\,\mathrm{Re}(cb^*\langle k_3\cdot k_2^*\rangle)$$

After dividing both numerator and denominator by $|a|\langle|k_1|^2\rangle$, the amplitude of the polarimetric coherence becomes:

$$|\gamma(\underline{\omega}_T,\underline{\omega}_P)| = \frac{\left|1 + \frac{b}{|a|}\frac{\langle k_1\cdot k_2^*\rangle}{\langle|k_1|^2\rangle} + \frac{c}{|a|}\frac{\langle k_1\cdot k_3^*\rangle}{\langle|k_1|^2\rangle}\right|}{\sqrt{\Lambda}} \quad (16)$$

$$\Lambda = 1 + \frac{|b|^2}{|a|^2}\frac{\langle|k_2|^2\rangle}{\langle|k_1|^2\rangle} + \frac{|c|^2}{|a|^2}\frac{\langle|k_3|^2\rangle}{\langle|k_1|^2\rangle} + \quad (17)$$
$$+ \frac{2\,\mathrm{Re}(ab^*\langle k_1\cdot k_2^*\rangle) + 2\,\mathrm{Re}(ac^*\langle k_1\cdot k_3^*\rangle) + 2\,\mathrm{Re}(cb^*\langle k_3\cdot k_2^*\rangle)}{|a|^2\langle|k_1|^2\rangle}$$

We refer to $|b|/|a|$ and $|c|/|a|$ as Reduction Ratios (*RedR*).

The pseudo targets are chosen in order to have small *RedR*. Hence, in the sum the elements containing the *RedR* are lowered. These terms are referred to as clutter terms. In eq.16-17 they are all of the elements except the ones with the sought component k_1 alone (i.e. $\left\langle |k_1|^2 \right\rangle$ that after the division become 1). There exist two typologies of clutter terms: cross-correlations and powers. The cross correlations are generally small, since for partial targets the components of $\underline{k}$ are likely to be uncorrelated. The power terms depend on the power of the clutter k_2 and k_3. Finally, when $\left\langle |k_1|^2 \right\rangle$ is higher than the clutter terms, the *RedR* combined with the division for $\left\langle |k_1|^2 \right\rangle$ makes the clutter terms negligible in the sum and the polarimetric coherence has unitary amplitude. If the component of interest is not dominant, the clutter terms start to have more influence in the final sum, lowering the coherence amplitude.

4) In conclusion, the detector is obtained setting a threshold on the coherence amplitude.

$$\left|\gamma(\underline{\omega}_T, \underline{\omega}_P)\right| < T \,. \tag{18}$$

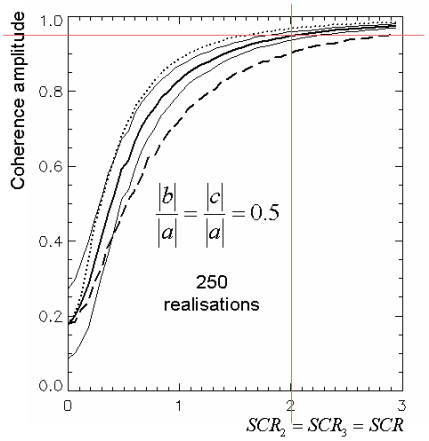

Figure 2. Coherence amplitude detector. Solid lines: mean inside the standard deviation boundaries for uncorrelated target-clutter. Dotted line: positive target-clutter correlation. Dashed line: negative target-clutter correlation. Average over 250 realizations with window 5x5.

Figure 2 presents the simulation of the coherence amplitude estimated as a stochastic process composed of a deterministic target k_1 (target to be detected) and two random variables, complex Gaussian zero mean (i.e. k_2 and k_3), independent each other. The solid lines show the mean value of the coherence (over 250 realizations) confined in the standard deviation boundaries. A 5x5 window and *RedR* of 0.5 are considered. Signal to Clutter Ratio (*SCR*) is defined as: $SCR_j = \left\langle |k_1|^2 \right\rangle \Big/ \left\langle |k_j|^2 \right\rangle$ with $j = 2,3$. In the plot, both the *SCR*s are increased simultaneously i.e. $SCR = SCR_2 = SCR_3$.

A. Bias Removal

The solid line in Figure 2 is obtained by considering the three components of the scattering vector $\underline{k}$ independently of each other, hence the cross correlation terms are almost zero (it is different from 0 just because the number of samples is finite). This condition is a good approximation for partial targets however, it could not be fulfilled for single (coherent) targets. The dotted and dashed line in Figure 2 present the case when the coherent target is correlated with the two clutter components, respectively in a constructive or destructive way. The amplitude of the correlation coefficient between the target and clutter is 0.65. In conclusion, correlation between the target and clutter creates bias on the coherence amplitude. The aim of this section is to remove this bias. Firstly, we recognize that the cross terms do not add useful information for the proposed detector. In the case of uncorrelated $\underline{k}$ components they merely add noise related to the finite averaging [25]. However, for high values of coherence, the bias introduced is not appreciable. On the other hand, when the $\underline{k}$ components are correlated, they bring bias that results in false alarms or miss detections. Consequently, the detector is improved and simplified when they are ignored.

In order to neglect them, the polarimetric coherence operator is substituted with another operator that works on the space of the target components power:

$$\left|\gamma_d(\underline{\omega}_T, \underline{\omega}_P)\right| = \frac{\left|\underline{\omega}_T^{*T} \langle [P] \rangle \underline{\omega}_P\right|}{\sqrt{\underline{\omega}_T^{*T} \langle [P] \rangle \underline{\omega}_T \cdot \underline{\omega}_P^{*T} \langle [P] \rangle \underline{\omega}_P}}, \tag{19}$$

where:

$$[P] = \begin{bmatrix} \left\langle |k_1|^2 \right\rangle & 0 & 0 \\ 0 & \left\langle |k_2|^2 \right\rangle & 0 \\ 0 & 0 & \left\langle |k_3|^2 \right\rangle \end{bmatrix}. \tag{20}$$

$$\left|\gamma_d(\underline{\omega}_T, \underline{\omega}_P)\right| = \frac{1}{\sqrt{1 + \frac{|b|^2}{|a|^2} \frac{\left\langle |k_2|^2 \right\rangle}{\left\langle |k_1|^2 \right\rangle} + \frac{|c|^2}{|a|^2} \frac{\left\langle |k_3|^2 \right\rangle}{\left\langle |k_1|^2 \right\rangle}}}. \tag{21}$$

The modified coherence in eq.21 will be referred to as the *detector*. The latter is dependent simply on the power components of the scattering vector $\underline{k}$.

Looking at eq.21, the lowering effect played by the *RedR* is clear. If the clutter power is lower than the target power the two terms on the denominator are negligible and $\left|\gamma_d\right| = 1$. The trend of the detector can be seen in Figure 3. Comparing Figure 2 and 3 the variance appears strongly reduced for low SCR's, moreover the two means look very close for values higher than 0.6. The difference for lower value is related with the coherence bias due to finite averaging. The bias is brought by the cross terms. Consequently, neglecting them the bias disappears (please note, for very high values of clutter the detector becomes 0). For uncorrelated components the cross terms result only in increasing variance.

The final expression of the detector set a threshold on eq.21:

$$\left|\gamma_d(\underline{\omega}_T, \underline{\omega}_P)\right| < T \,. \tag{22}$$

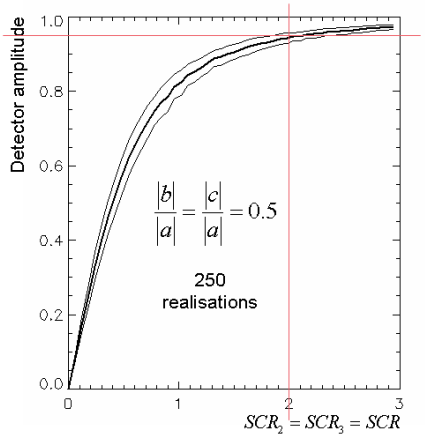

Figure 3. Detector: mean over 250 realizations inside the standard deviation boundaries. Window 5x5.

B. Detector Interpretation

In order to give an intuitive view of the detector, Figure 4 represents the filtering effect as a simple schematic. The vertical bars stand for the power of the scattering vector components. After the change of basis that makes $\underline{\omega}_T = [1,0,0]^T$, k_1 represents the target to detect and k_2, k_3 are the clutter.

The final image (as interpreted by the final detector) is obtained as the incoherent sum of the three components. The image formation behaves similar to a filter (more precisely it is a scalar projection). The first row of any example (i.e. $\underline{\omega}_T$ filter) is ideal and deletes completely the orthogonal clutter components.

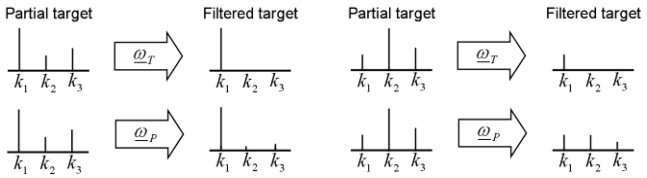

(a) detection achieved (b) no detection achieved

Figure 4. Visual explanation of the filter with target and pseudo target.

The second row (i.e. $\underline{\omega}_P$ filter) results in a linear combination of the sought component (slightly lowered) plus a small amount of the orthogonal ones. In (a) the match between the target and pseudo target final image is high, since the power in the two images is similar. This is not true in (b), since the $\underline{\omega}_P$ image has much more power than the $\underline{\omega}_T$ one, hence in the normalization in eq.21 the $\underline{\omega}_P$ image significantly lowers the coherence.

III. PARAMETERS SELECTION

A. Reduction Ratios (RedR) and Threshold

The detector (as expressed in eq.21) is a stochastic process [26]. In order to optimally set the threshold, and assess the probability of false alarms and miss detection, the probability density function (pdf) of the detector is required. Its evaluation is out of the scope of this first paper, hence we are looking for an expression of the detector independent of the statistical realization. For this purpose, the finite average operator $\langle . \rangle$ is substituted with the expected value *E*[.]. Considering the detector works with a high value of coherence, the latter assumption is easily fulfilled for a 5x5 window.

$$|\gamma_d(\underline{\omega}_T, \underline{\omega}_P)| \approx \frac{1}{\sqrt{1+\frac{|b|^2}{|a|^2}\frac{1}{SCR_2}+\frac{|c|^2}{|a|^2}\frac{1}{SCR_3}}} \tag{23}$$

$$SCR_2 = E\left[|k_1|^2\right] / E\left[|k_2|^2\right],\ SCR_3 = E\left[|k_1|^2\right] / E\left[|k_3|^2\right] \tag{24}$$

Once the pseudo target $\underline{\omega}_P$, is fixed, eq.23 is an expression related exclusively to the *signal to clutter ratio* (*SCR*).

Figure 5 represents the results, where the value of the *RedR* is varied. Please note the mean curves in Figure 3 overlap almost perfectly with the one in Figure 5 (for *RedR*=0.5). The detector presents no bias and the threshold can be set on the deterministic detector to the base of the *SCR* to be detected. Figure 5 also allowed some consideration of the *RedR*. The detector increases when the ratio is reduced (the clutter terms are lower). Regarding the choice of the ratio, a small value reduces the variance (since we work with higher values of modified coherence), however the range of discrimination between targets is reduced (the curve flattens earlier). Considering we want to detect targets with a *SCR* higher than 1.5-2 a good choice for the ratio is 0.5 (that makes the threshold set around 0.95).

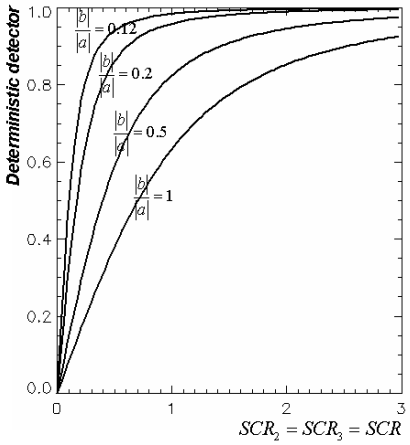

Figure 5. Deterministic detector (reduction ratio varied).

Once the *RedR* is fixed it is possible to set the threshold. For strong targets, the discrimination is quite easy, so the minimization of false alarm is the key point. Hence, a high *SCR* can be chosen (this leads to a higher threshold). On the other hand, if embedded (e.g. foliage penetration FOLPEN) or weak targets (with low total backscattering) are to be detected, a lower *SCR* must be selected (consequently a lower threshold). The effect of the threshold choice is clearly visible in the validation section. Please note, the detection ability is

not related directly with the total power scattered by the target (span of the scattering matrix), but exclusively with the reciprocal weight of the scattering components. The threshold reduction for weak targets is related to the noise effect, which confuses the polarimetric characteristics. In order to check this property a simulation was performed with no clutter and just additive thermal uncorrelated noise. The results is that the threshold is required to be lower than 0.98 to detect a target of interest with SNR (over the window) of about 1dB and, less than 0.88 for -10dB SNR.

B. Pseudo Target Selection

In the previous section a tacit hypothesis is employed: $|b|=|c|$. The aim of this section is to evaluate the effects of $|b|\neq|c|$. The components of $\underline{\omega}_P$ are not independent, since $|a|^2+|b|^2+|c|^2=1$, because $\underline{\omega}_P$ is a normalized vector. In order to show the importance of a good choice of *b* and *c*, an example is presented. It is given that $\underline{k}=\kappa[a',b_0,0]$, $\underline{\omega}_P=[a,0,c_0]$ and $\underline{\omega}_T=[1,0,0]$, where $|b_0|=\sqrt{1-|a'|^2}$, $|c_0|=\sqrt{1-|a|^2}$. The detector will be:

$$|\gamma_d(\underline{\omega}_T,\underline{\omega}_P)|=\frac{1}{\sqrt{1+\frac{0}{|a|^2}\frac{|b_0|^2}{|a'|^2}+\frac{|c_0|^2}{|a|^2}\frac{0}{|a'|^2}}}=1 \quad (25)$$

Basically, the orthogonality (or in general the geometrical relationship) between the clutter components of $\underline{k}$ and $\underline{\omega}_P$ can bias the detector. In order to remove this bias we want to find a relation between *b* and *c* that makes the detector not biased. It can be demonstrated that this choice is $|b|=|c|$. In order to show the feasibility, we consider a general target as $\underline{k}=\kappa[a',b',c']$. After algebraic manipulations we have

$$|\gamma_d(\underline{\omega}_T,\underline{\omega}_P)|=\frac{1}{\sqrt{1+\frac{|b|^2}{|a|^2|a'|^2}\left(|b'|^2+|c'|^2\right)}} \quad . \quad (26)$$

Eq.26 states that the total (normalized) power of the clutter components is all contained in $|b'|^2+|c'|^2$, it does not matter which is the strongest component between *b'* and *c',* the bias is removed.

C. Detector Implementation

The expression obtained in eq.21 is still dependent on the basis used to express the vectors $\underline{\omega}_T$ and $\underline{\omega}_P$. In that basis the target to detect is present exclusively in the k_1 component (i.e. k_2, k_3 represent the clutter). If three unitary vectors $\underline{e}_1=[1,0,0]^T$, $\underline{e}_2=[0,1,0]^T$ and $\underline{e}_3=[0,0,1]^T$ are introduced, the power of target and clutter (in the basis that makes $\underline{\omega}_T=[1,0,0]^T$) can be written as:

$$P_T=\left\langle\left|\underline{k}^T\cdot\underline{e}_1\right|^2\right\rangle,\ P_{C2}=\left\langle\left|\underline{k}^T\cdot\underline{e}_2\right|^2\right\rangle \text{ and } P_{C3}=\left\langle\left|\underline{k}^T\cdot\underline{e}_3\right|^2\right\rangle. \quad (27)$$

Consequently, eq.21 can be modified:

$$|\gamma_d(\underline{\omega}_T,\underline{\omega}_P)|=\frac{1}{\sqrt{1+\frac{|b|^2}{|a|^2}\frac{P_{C2}}{P_T}+\frac{|c|^2}{|a|^2}\frac{P_{C3}}{P_T}}} \quad . \quad (28)$$

The change of basis that makes $\underline{\omega}_T=[1,0,0]^T$ can be found by solving a system of equations.

An easier way to obtain eq.28, starting from any set of basis, considers the Gram-Schmidt ortho-normalization [27], which sets $\underline{\omega}_T$ as one axis of a new basis set for the target space *SU*(3). The new basis will be composed by three unitary vectors $\underline{u}_1=\underline{\omega}_T$, $\underline{u}_2=\underline{\omega}_{C2}$ and $\underline{u}_3=\underline{\omega}_{C3}$. Where $\underline{\omega}_{C2}$ and $\underline{\omega}_{C3}$ are two orthogonal components to $\underline{\omega}_T$ necessary to build up the three diagonal elements of the coherency matrix. Hence, P_T, P_{C1} and P_{C2} are calculated as:

$$P_T=\left\langle\left|\underline{k}^T\cdot\underline{u}_1\right|^2\right\rangle,\ P_{C2}=\left\langle\left|\underline{k}^T\cdot\underline{u}_2\right|^2\right\rangle \text{ and } P_{C3}=\left\langle\left|\underline{k}^T\cdot\underline{u}_3\right|^2\right\rangle. \quad (29)$$

With this operation we complete the process that makes the detector a mathematical operator, where the optimum *RedR* are set on the base of the *SCR* and bias removal as explained in the previous sub-sections.

D. Specialization to multiple reflection and oriented dipole

The mathematical formulation shows that the algorithm is able to detect any single target as long as its polarization fork (in particular the two Co-Pol Nulls) or Huynen parameters are known. In order to test the algorithm over real targets the detection is specialized for multiple reflections (odd and even bounce) and oriented dipoles (horizontally and vertically). These four typologies of target are selected because of the relatively easy association with real targets on a radar image.

Figure 6 represents the Poincaré sphere with characteristic polarizations for the targets considered.

IV. VALIDATION

In order to validate and test the potential of the detector, it is applied on a fully polarimetric L-band SAR dataset. In all the mathematical formulation the frequency is not involved, and the detector is not directly frequency dependent (the dependence is related with changes in the target when the frequency is varied). The choice of the frequency can be related to the target to detect. L-band presents an interesting setting, based on its ability to penetrate foliage (FOLPEN) capability [28]. The dataset were acquired by the DLR (German Aerospace Agency) during the SARTOM campaign in 2006 [29], with the E-SAR airborne system.

One aim of the campaign was target detection beneath foliage, hence a set of artificial targets were deployed in open fields and inside the forest. For this reason, the dataset presents an ideal test scenario. As explained before, the threshold used is higher for open fields than for forested areas.

Figure 7 presents the detection on an open field. The L-band reflectivity in (a) HH and (d) HV polarizations are given as comparison. Moreover, in (a) there are markers to identify particular targets. A jeep is deployed in the middle of the image (Mercedes Benz 250 GD, also named 'Wolf') and the two bright points above and below the jeep are trihedral corner reflectors used for calibration (top 149cm; bottom 70cm). Finally, on the bottom of the image there is a vertical metallic net (these defenses were used to delimitate areas). The range direction is along the vertical axes (bottom to top). The detector masks show where the targets are located, where the intensity is related to the amplitude of the detector (modified coherence amplitude), scaled to the base of the threshold. The detector parameters are those proposed in the previous section. The algorithm detects the trihedral corner reflectors as a source of odd bounce (b). The jeep presents mainly even-bounces (presumably with the ground) (c). Moreover, we can see some even bounces on the forest edge, due to the trunk-ground double bounce effect that is stronger at the edge where it is exposed and has less attenuation from the canopy.

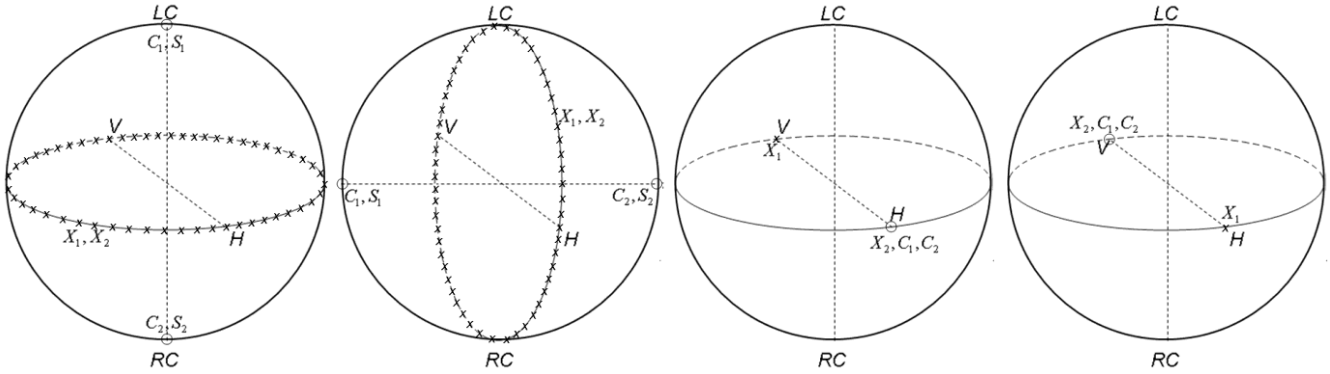

Figure 6. Poincaré representation of single target detected (a) odd-bounce; (b) even-bounce; (c) vertical dipole; (d) horizontal dipole.

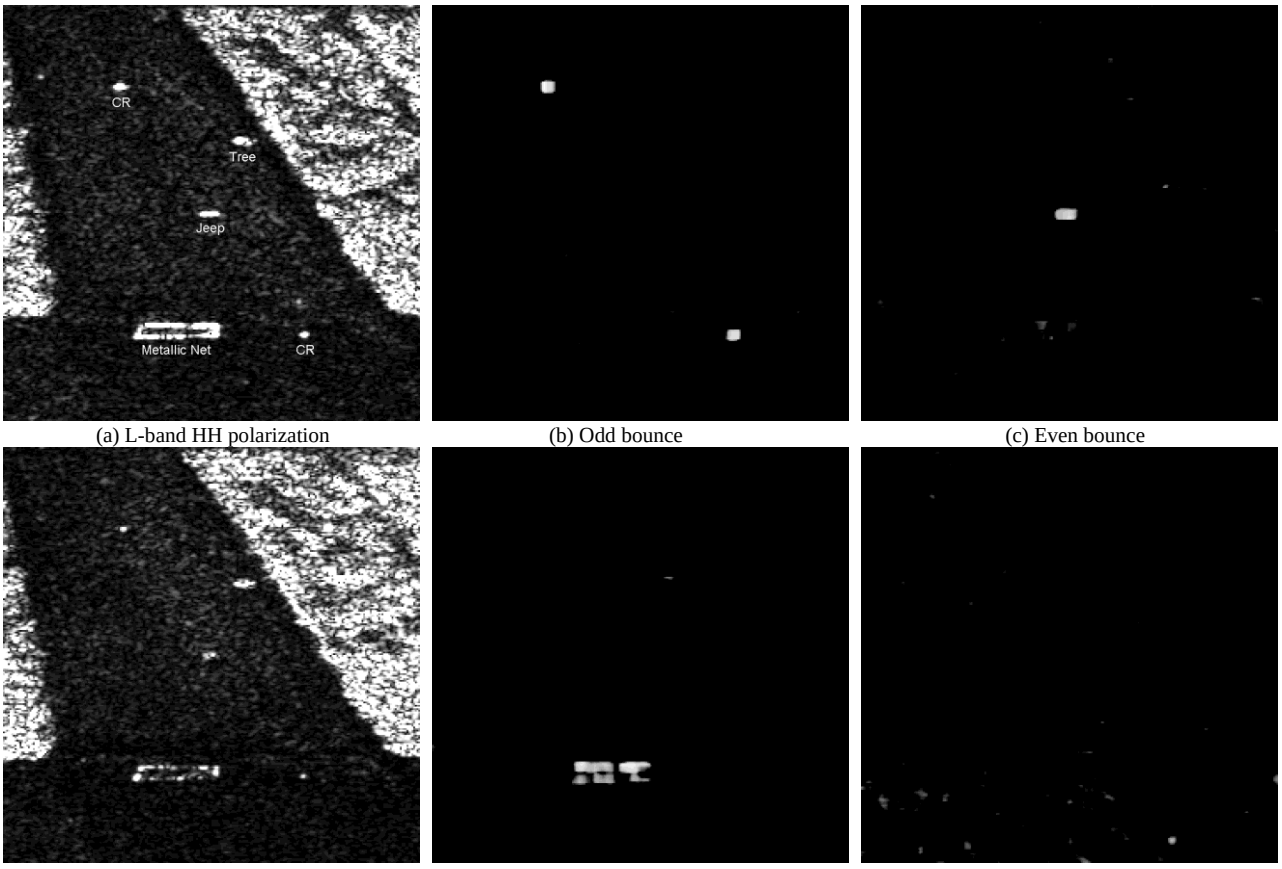

(a) L-band HH polarization (b) Odd bounce (c) Even bounce

(d) L-band HV polarization (e) Horizontal dipoles (f) Vertical dipoles

Figure 7. Detection over open field area. (a) L-band HH polarization with markers for some targets. (b) Mask for odd bounce detection (5x5); (c) Mask for even bounce detection. (d) L-band HV polarization. (e) Mask for horizontal dipole detection; (f) Mask for vertical dipole detection. The intensity of the masks is related to the detector amplitude.

Finally, the net has a strange polarimetric behavior. Due to the mesh size (that goes from around 10cm on the bottom to 30cm on the top) the lower part is roughly similar to a wall for the 23cm wavelength radiation. It creates weak double bounce with the ground, and strong horizontal dipoles (e). In fact, due to the radar geometry the return from the net vertical dipole is much lower (f). Regarding the oriented dipole detection (e-f), the corner reflectors disappear completely (they are surfaces). Moreover, the horizontal branches of the isolated tree are visible (i.e. big horizontal branches throughout the canopy), as well as some vertical structure on the ground (i.e. bushes with big wooden vertical stems). A ground campaign was performed in order to check the existence of the targets detected – in the interests of brevity, we do not show the photographs of the targets.

In Figure 8, the algorithm is tested for detection beneath foliage (FOLPEN). The targets are three trihedral corner reflectors (top: 149cm, bottom left: 70cm, bottom right: 90cm). In the reflectivity images (a,d) the CRs are not recognizable, conversely they are easily detected in (b) the odd bounce mask (i.e. triple bounces).

Considering the threshold now is low, some points on the bare soil are detected as sources of single-bounce (top of (b)). These are not false alarm since the bare soil can be approximated as a single bounce Bragg surface. Regarding the even bounce (c), it detects some trunk-ground double bounce, especially in proximity of the forest clearing (that runs horizontally separating the top and bottom CRs). Finally, it is not possible to detect particular oriented dipoles in the forest (e-f). This is in line with the RVoG model for L-band, where the forest structures are random and do not present preferential orientations.

A. Polarimetric Characterization of Detected Targets

The algorithm development is based on the polarization fork (or Huynen parameters), this means that the detectors is mainly aimed at single targets. In fact an ideal polarization fork can not be defined for a partial target [24, 30]. In order to check this property, the entropy for the detected points over the whole dataset is estimated and the normalized histogram is presented in Figure 9.b. The entropy is generally lower than 0.5 indicating targets with single scatterer (coherent) behavior. As a comparison, in Figure 9.a the entropy for all the pixels is depicted, showing much higher values.

B. Comparison with PWF

The aim of this section is to have a comparison with one of the most commonly used polarimetric target detector, i.e. Polarimetric Whitening Filter PWF [4]. Briefly, the PWF uses the polarization to filter the images reducing (optimally) the speckle. Practically, all the pixels interpreted as affected by speckle are strongly reduced. PWF is nowadays considered one of the most powerful detectors which do not require a priori information about the statistics of the target. Since our detector does not require statistical a priori hypothesis as well, the comparison is worthwhile.

Figure 10.a and 10.b shows the results of the PWF for the two areas already presented. In the open field the performances are comparable (a). Both the techniques detect jeep, net and corner reflectors. However, PWF performs only target detection, and not target classification. On the other hand, in a more critical situation as in a forested scenario, the PWF fails in detecting one CR (bottom left: 70cm). This is due to the fact that the embedded targets can be affected by speckle even if they are coherent itself (because of the surrounding clutter and non-uniform attenuation). Regarding the weak targets, PWF is based on a threshold over the backscattered power, hence weak targets are lost. The new detector proposed here is based on the weight of the target components, hence it can detect low backscattering targets as long as they are polarimetrically characterized.

CONCLUSION

A target detector was developed based on the unique polarimetric fork (PF) of the single target (similarly the Huynen parameters or the α angle can be used). The mathematical formulation carried out is general, and so can be applied for any single target of interest (as long as the PF is known). The validation was achieved over two categories of targets: multiple reflection and oriented dipoles. In both cases, the results are in line with the expected physical behavior of the targets. A supplementary theoretical validation and evaluation is carried out in where the algorithm is compared with the well-known Polarimetric Whitening Filter (PWF), showing better performances for embedded targets.

This paper presents the first attempt to use polarimetric filters to make a sensitivity analysis aimed at target detection. Regarding the application of the detector, the targets that can be investigated are not exclusively artificial. For instance, if the polarimetric model of a particular single target is available (we could eventually obtain it from a dataset), the algorithm can be used to recognize similar features that appear elsewhere in another dataset.

ACKNOWLEDGE

This project forms part of the SARTOM project run by eOsphere Ltd and funded by DSTL. The authors would like to thank Nick Walker of eOsphere for moral and technical support of the algorithm development.

The authors want to thank Matthew Brolly from the University of Edinburgh, School of Geosciences, for his help in the preparation of the paper.

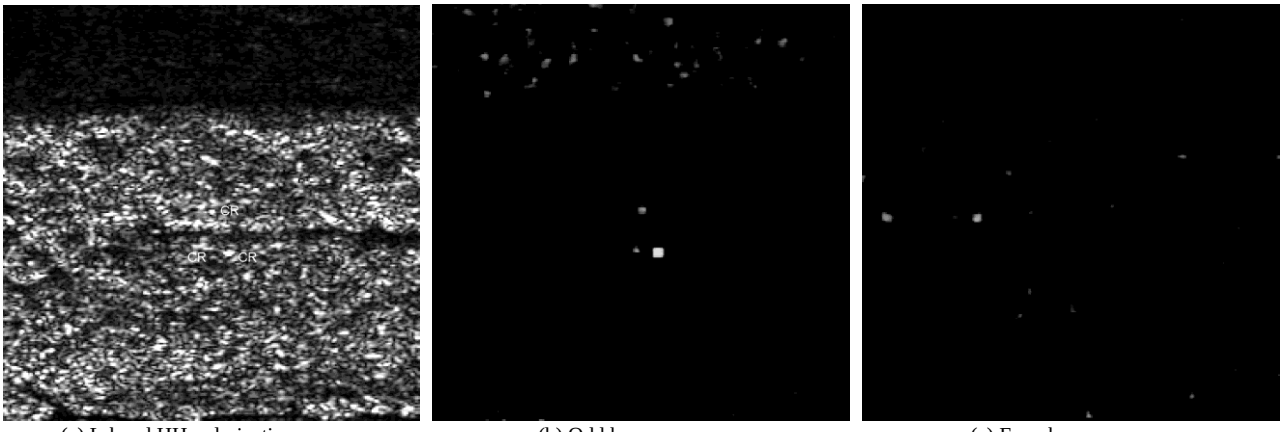

(a) L-band HH polarization (b) Odd bounce (c) Even bounce

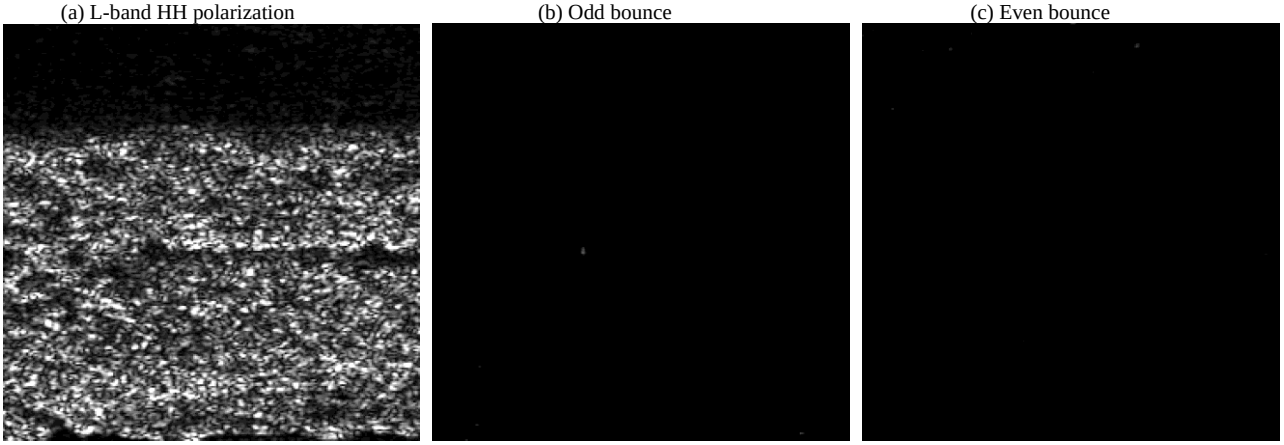

(d) L-band HV polarization (e) Horizontal dipoles (f) Vertical dipoles

Figure 8. Detection over forested area. (Same as Figure 7).

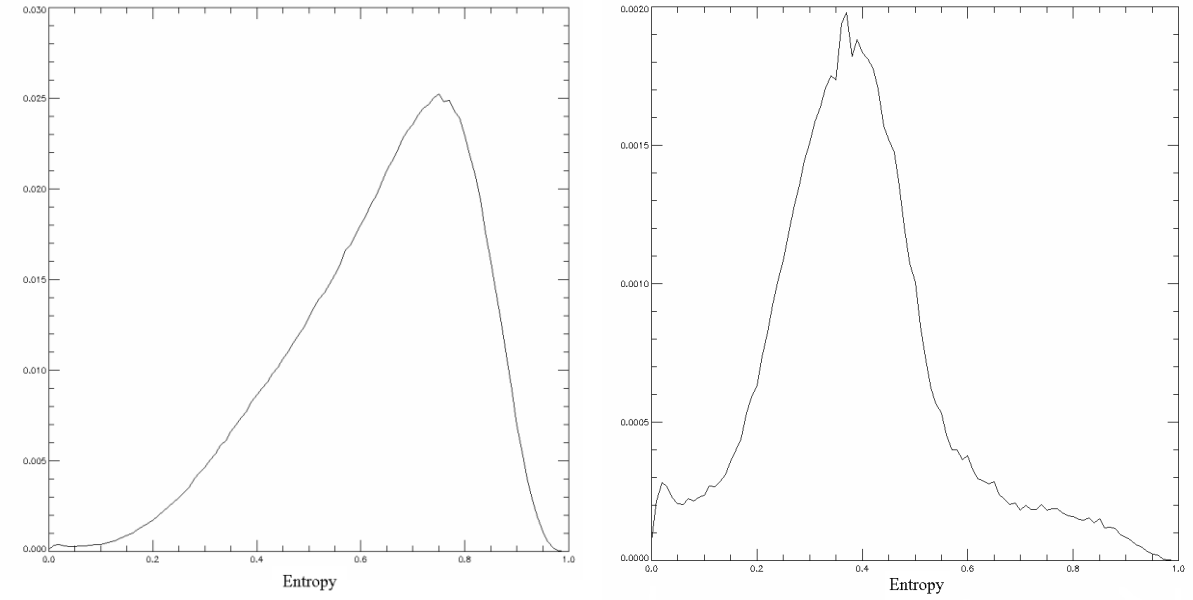

(a) Entropy total image (b) Detected points (high threshold)

Figure 9. Histogram of the entropy for (a) total image and (b) detected mask

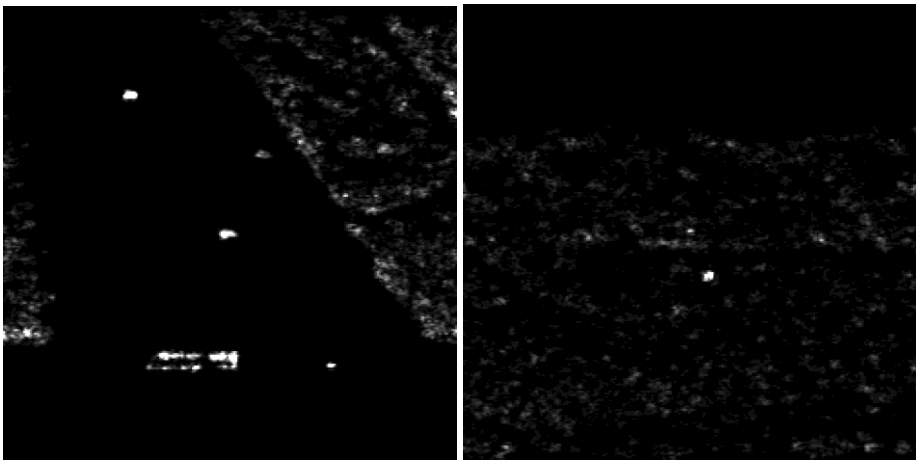

(a) PWF open field (b) PWF forested area

Figure 10. PWF: (a) open field; (b) forested area.

REFERENCE

[1] L. M. Novak, G. J. Owirka, and A. L. Weaver, "Automatic Target Recognition Using Enhanced Resolution SAR Data," *IEEE Trans. Aerospace and Electronic Systems*, vol. 35, pp. 157-175, 1999.

[2] J. Li and E. G. Zelnio, "Target detection with synthetic aperture radar," *IEEE Transactions on Aerospace and Electronic Systems*, vol. 32, pp. 613-627, 1996.

[3] L. M. Novak, G. J. Owirka, and C. M. Netishen, "Performance of a High-Resolution Polarimetric SAR Automatic Target Recognition System," *The Lincolm Laboratory Journal*, vol. 6, pp. 11-24, 1993.

[4] L. M. Novak, M. C. Burl, and M. W. Irving, "Optimal Polarimetric Processing for Enhanced Target Detection," *IEEE Trans. Aerospace and Electronic Systems*, vol. 20, pp. 234-244, 1993.

[5] S. R. Cloude, D. G. Corr, and M. L. Williams, "Target Detection beneath Foliage Using Polarimetric Synthetic Aperture Radar Interferometry " *Waves in Random and Complex Media*, vol. 14, pp. 393 - 414, 2004.

[6] G.D. De Grandi, J.-S. Lee, and D. L. Schuler, "Target Detection and Texture Segmentation in Polarimetric SAR Images Using a Wavelet Frame: Theoretical Aspects," *IEEE Transactions on Geoscience and Remote Sensing*, vol. 45, pp. 3437-3453, 2007.

[7] G. Margarit, J.J. Mallorqui, and X. Fabregas, "Single-Pass Polarimetric SAR Interferometry for Vessel Classification," *IEEE Transactions on Geoscience and Remote Sensing*, vol. 45, pp. 3494-3502, 2007.

[8] W. M. Boerner, "Basics of Radar Polarimetry," *RTO SET Lecture Series*, 2004.

[9] I. H. Woodhouse, *Introduction to Microwave Remote Sensing* CRC Press, Taylor & Frencies Group, 2006.

[10] S. R. Cloude and E. Pottier, "A review of target decomposition theorems in radar polarimetry," *IEEE Transaction on Geoscience and Remote Sensing*, vol. 34, pp. 498-518, 1996.

[11] E. M. Kennaugh and R. W. Sloan, "Effects of Type of Polarization On Echo Characteristics," 17 March 1952.

[12] S. R. Cloude, "Polarimetry: The characterisation of Polarisation Effects in EM Scatterinig," in *Electronics Engineering Department*, vol. PhD. York: University of York, 1987, pp. 161.

[13] J. R. Huynen, "Phenomenological theory of radar targets," vol. Ph.D. Delft: Technical University The Netherlands, 1970.

[14] W. L. Cameron and L. K. Leung, "Feature Motivated Polarization Scattering Matrix Decomposition," *Record of the IEEE International Radar Conference*, pp. 549-557, 1990.

[15] E. Krogager, "Aspects of Polarimetric Radar Imaging," vol. PhD. Lyngby, DK: Technical University of Denmark, 1993

[16] W. M. Boerner, M. B. El-Arini, C. Y. CHAN, and P. M. Mastoris, "Polarization Dependence in Electromagnetic Inverse Problems," *IEEE Trans. on Antennas and Propagation*, vol. 29, pp. 262 - 271, 1981.

[17] W.M. Boerner, W.L. Yan, A.Q. Xi, and Y. Yamaguchi, "The Characteristic Polarization States for the Coherent and Partially Polarized Case," *Proceedings of the IEEE Antennas and Propagation Conf, ICAP*, vol. 79, pp. 1538-1550, 1991.

[18] K. P. Papathanassiou, "Polarimetric SAR Interferometry," in *Physics*, vol. PhD: Technical University Graz, 1999.

[19] K. P. Papathanassiou and S. R. Cloude, "Single-Baseline Polarimetric SAR Interferometry," *IEEE Transaction on Geoscience and Remote Sensing*, vol. 39, pp. 2352-2363, 2001.

[20] S. R. Cloude, *Lie groups in electromagnetic wave propagation and scattering: Electromagnetic symmetry*: CE Baum and He Kritikos, 1995

[21] S. R. Cloude and E. Pottier, "An Entropy Based Classification Scheme for Land Applications of Polarimetric SAR," *IEEE Transaction on Geosciance and Remote Sensing*, vol. 35, pp. 68-78, 1997.

[22] G. A. Deschamps and P. Edward, "Poincare Sphere Representation of Partially Polarized Fields," *IEEE*

Trans. on Antennas and Propagation, vol. 21, pp. 474-478, 1973.

[23] Y. Dong and B. Forster, "Understanding of Partial Polarization in Polarimetric SAR Data," *International Journal of Remote Sensing*, vol. 17, pp. 2467-2475, 1996.

[24] J. van Zyl, C. Papas, and C. Elachi, "On the optimum polarizations of incoherently reflected wave," *IEEE Transactions on Antennas and Propagation*, vol. AP-35, pp. 818-825, 1987.

[25] R. Touzi, A. Lopes, J. Bruniquel, and P. W. Vachon, "Coherence estimation for SAR imagery," *IEEE Transaction on Geosciences and Remote Sensing* vol. 37, pp. 135-149, 1999.

[26] G. Franceschetti and R. Lanari, *Synthetic Aperture Radar Processing* CRC Press 1999.

[27] G. Strang, *Linear Algebra and its Applications*, Third ed: Thomson Learning, 1988.

[28] J. G. Fleischman, S. Ayasli, and E. M. Adams, "Foliage attenuation and backscatter analysis of SAR imagery," *IEEE Trans. on Aerospace and Electronic Systems*, vol. 32, pp. 135-144, 1996.

[29] R. Horn, M. Nannini, and M. Keller, "SARTOM Airborne Campaign 2006: Data Acquisition Report," DLR-HR-SARTOM-TR-001 December 2006.

[30] S. R. Cloude, "Uniqueness of target decomposition theorems in radar polarimetry," *Direct and Inverse Methods in Radar Polarimetry*, pp. 267-296, 1992.

Armando Marino received the MSc in Telecommunication Engineering, Universita' di Napoli "Federico II" in 2006. In 2006, he joined the High Frequency and Radar Systems Department (HR), German Aerospace Centre (DLR), Oberpfaffenhofen, where he developed his MSc thesis, which focused on SAR multi pass retrieval of forest parameters.
Since February 2007, he is pursuing the Ph.D. degree at the University of Edinburgh (School of Geosciences), Edinburgh, UK, in the field of polarimetric SAR interferomery. His main research interest is target detection and POLInSAR applied on forested areas.

Shane R. Cloude (M'87–SM'96–F'01) received the B.Sc. degree from the University of Dundee, Dundee, U.K., in 1981, and the Ph.D. degree from the University of Birmingham, Birmingham, U.K., in 1987. He was a Radar Scientist at the Royal Signals and Radar Establishment (RSRE), Great Malvern, U.K., until 1987. Following this, he held teaching and research posts at the University of Dundee, the University of York, U.K., and the University of Nantes, France, before taking on his present role in 1996. He is currently Director and Senior Scientist with Applied Electromagnetic Consultants (AELc), Edinburgh, U.K., undertaking contract research on a range of problems associated with radar remote sensing.
Dr Cloude is a Fellow of the IEEE, the Alexander von Humboldt Society in Germany and honorary Fellow of the School of Geosciences, University of Edinburgh.

Iain H. Woodhouse is a Senior Lecturer in Radar Remote Sensing at the School of GeoSciences, University of Edinburgh. His expertise is in the retrieval of biophysical properties of vegetation using active remote sensing, specifically synthetic aperture radar (SAR) and lidar. A key focus of his approach is the linking of observational models with process models. He is a principal investigator on a number of projects related to quantitative measurements of forests from remote sensing, funded by NERC, DTI, DSTL and the Forestry Commission. He is also a member of the NERC Earth Observation Director's Advisory Board, the Group on Earth Observations (GEO) Capacity Building Committee and a non-executive director of Ecometrica Ltd. He was a founding member of the Edinburgh Earth Observatory (EEO), a Research Group within the School of GeoSciences. Iain has a PhD from the Heriot-Watt University, an MSc in Remote Sensing from Dundee University and a BSc(hons) from the University of Edinburgh. He has also worked at the Marconi Research Centre and Wageningen University. In 1999 he moved to the University of Edinburgh.